Seismotectonic Snapshots: The 18 March 2020 M_w 5.7 Magna, 31 March 2020 M_w 6.5 Stanley, and 15 May 2020 M_w 6.5 Monte Cristo Intermountain West Earthquakes

Steven G. Wesnousky[*1]

Abstract

Seismological characteristics of the 18 March 2020 M_w 5.7 Magna, 31 March 2020 M_w 6.5 Stanley, and 15 May 2020 M_w 6.5 Monte Cristo Intermountain West earthquakes are largely consistent with expectations arising from observations accumulated over the ∼ 40 yr since implementation and subsequent growth of seismic networks in the broad region. Each occurred within a zone of relatively elevated seismicity, active faults, and geodetically observed strain accumulation. Aftershock distributions in each are confined primarily to depths of < 15 km, and the total number of aftershocks correlates with the relative size of the events. In each case, the number per day decays exponentially in the days following the mainshock. None of the mainshocks was preceded by a foreshock sequence that delivered a plausible warning of the impending earthquakes. With respect to tectonics, each earthquake brings new insights. The Stanley and Monte Cristo earthquakes are at the margins of geodetically defined regions of right-lateral transtension, though the pattern of faulting in each region is markedly different. The strike-slip mechanism of the Stanley earthquake stands in contrast to the zone of normal major range bounding faults and historical earthquake ruptures that characterize the region in which it occurred and is the first relatively well instrumented event to show a rupture extending northward through the Trans-Challis fault system. The Magna event has been interpreted to represent low-angle normal slip near the base of a listric Wasatch range bounding fault (Pang *et al.*, 2020). The east-striking left-lateral Monte Cristo earthquake within the Walker Lane is in contrast to the major northwest-striking right-lateral faults that dominate the area, though predictable from prior regional mapping. Surface rupture reportedly accompanied only the Monte Cristo earthquake, though its trace does not clearly follow the zone of aftershocks.

Introduction

The United States Intermountain West produced three significant large earthquakes in 2020 (Fig. 1). The M_w 5.7 Magna, Utah, the M_w 6.5 Stanley, Idaho, and the M_w 6.5 Monte Cristo range, Nevada, earthquakes are the largest registered in the last several decades or more in each of the areas where they occurred. The earthquakes are reminders of the seismic hazard that accompanies the ongoing diverse tectonic processes across this vast area. Here, each is briefly described in context of contemporary seismicity of $\mathbf{M} > 2$ documented in the Advanced National Seismic System (ANSS) Comprehensive Earthquake Catalog (U.S. Geological Survey [USGS], 2020a), the historical and geological record of prior large and nearby earthquakes, and the tectonic framework of the surrounding regions.

Earthquake Locations in General Tectonic Framework

The appellation Intermountain West here refers to the continental western United States located between the Sierra Nevada and Cascade mountain ranges in the west and the Wasatch Range and Rocky Mountains in the east (Fig. 1). The area encompasses three distinct regions distinguished by different orientations and styles of active faults. Each region was host to one of the 2020 earthquakes.

1. Center for Neotectonic Studies and Nevada Seismological Laboratory, University of Nevada, Reno, Nevada, U.S.A.

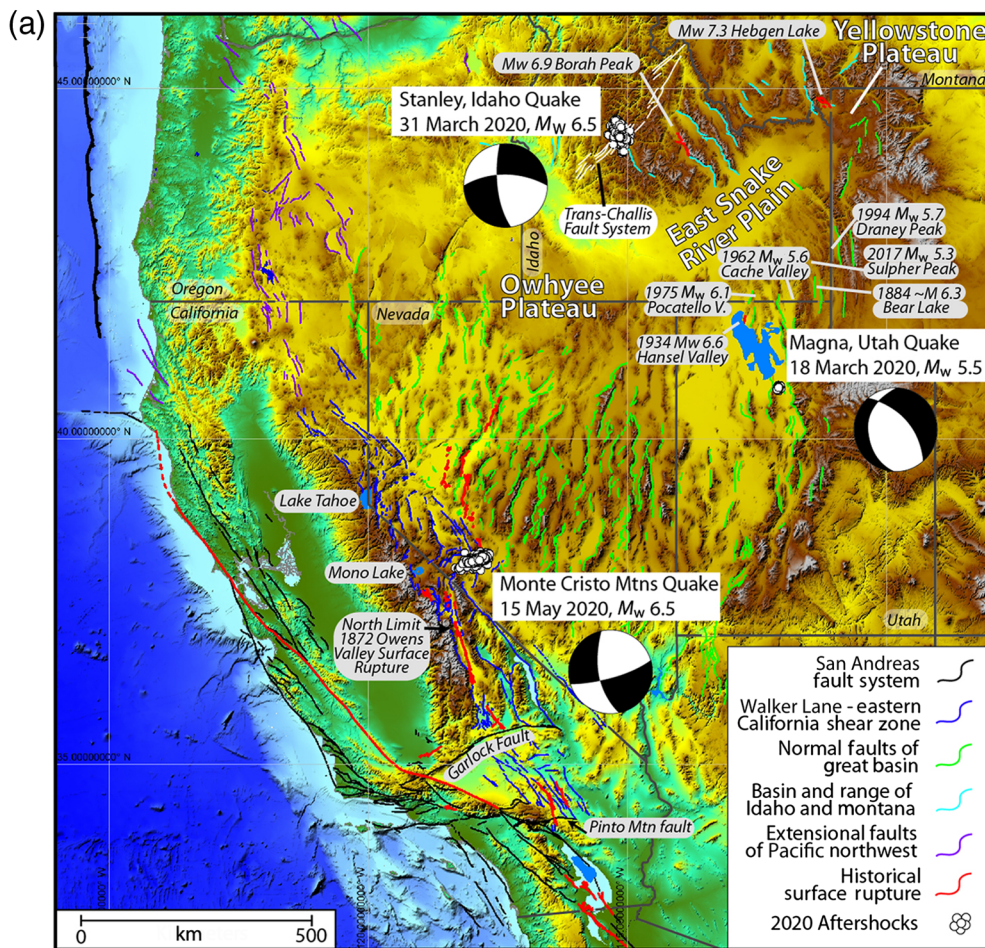*Corresponding author: wesnousky@unr.edu

Figure 1. (a) Aftershocks (white dots) and mainshock focal mechanisms of three significant 2020 earthquakes (each labeled) in the Intermountain West shown on physiographic map displaying distribution of major active faults (colored lines). (b) Aftershock sequences shown in relation to epicenters of **M ≥ 2** earthquakes across western United States reported in Advanced National Seismic System (ANSS) Comprehensive Earthquake Catalog (ComCat) since 1930 (USGS, 2020a). Dashed polygons encompass seismicity used in regional seismicity analysis. Physiography is from Becker et al. (2009). Fault distribution modified from the U.S. Geological Survey (USGS) Fault and Fold Database (USGS, 2020b) and earthquake data taken from ANSS ComCat (USGS, 2020a). The color version of this figure is available only in the electronic edition. (*Continued*)

The zone of northwestward-striking (blue) faults along the eastern edge of the Sierra Nevada is right-lateral, largely strike-slip and associated with higher levels of instrumentally recorded seismicity than adjacent regions (Fig. 1). Cumulative right-lateral offsets across the zone from ∼12–8 Ma register between ∼30 and 100 km, generally decreasing from south to north (e.g., Faulds et al., 2005; Wesnousky, 2005a; Oldow et al., 2008). The zone of faults is commonly referred to as the eastern California shear zone in the southeast and the Walker Lane as it progresses northwestward from California into Nevada. The M_w 6.5 Monte Cristo earthquake occurred in the Walker Lane. Ongoing right-lateral shear across the Walker Lane at the latitude of the earthquake is ∼8 mm/yr (Bormann et al., 2016).

East of the Walker Lane, the pattern and style of faulting abruptly changes. The faults (green in Fig. 1) strike north to northeast, generally exhibit normal displacement, and the displacements have resulted in the distinct basin and range topography from which the region derives its name: the Basin and Range province (Fig. 1 and, e.g., Stewart, 1978). Estimates of the cumulative extension that has accompanied development of the basin and ranges since initiation in the early Miocene are on the order of 50–100 km at ∼40° N (Thompson, 1959; Hamilton and Meyers, 1966; Stewart, 1971). Instrumentally recorded seismicity is distributed unevenly across the province: generally broad, diffuse, and at relatively low rates of occurrence within the interior of the province relative to higher rates at the margins adjacent to the Wasatch and within the Walker Lane. The pronounced belt (zone) of seismicity at the eastern margin of the Basin and Range initially documented by Cook and Smith (1967) is now commonly referred to as the Interseismic Mountain Belt following the early efforts of
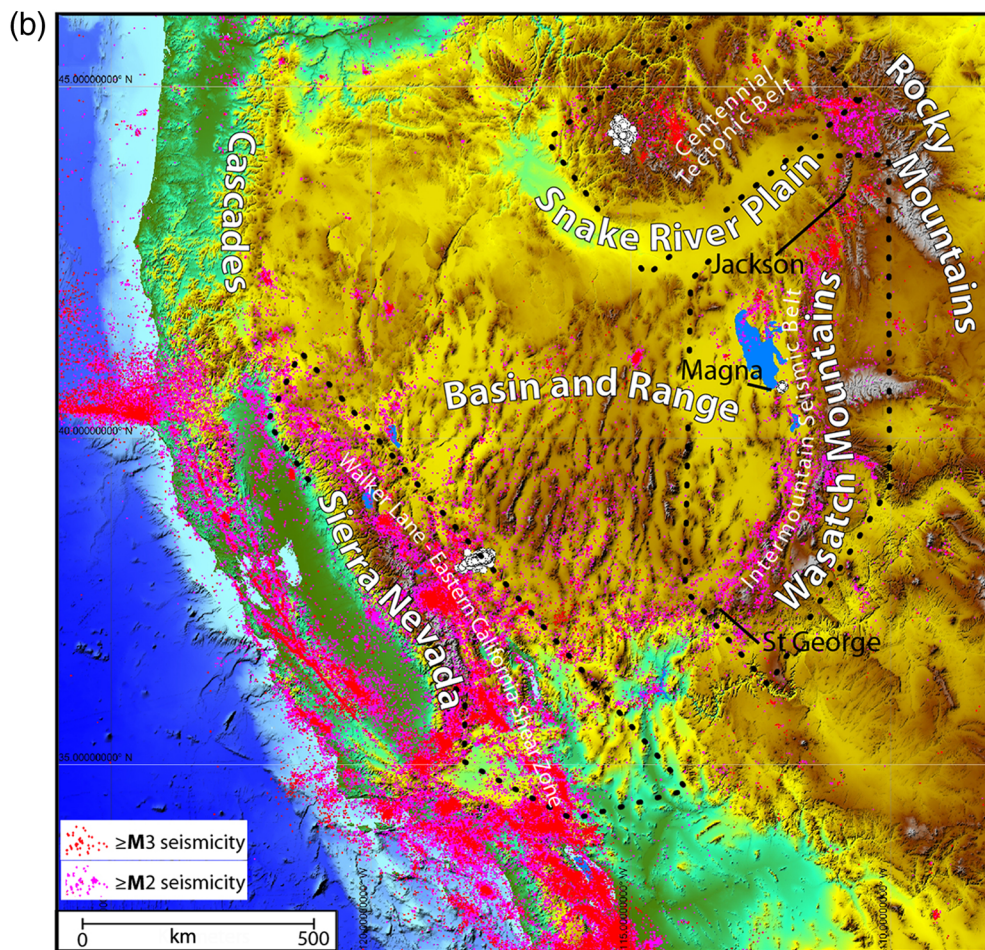
Figure 1. Continued

Sbar *et al.* (1972) and Smith and Sbar (1974) to place the zone in a geophysical and tectonic framework. Abrupt geophysical and tectonic changes from west to east across the belt include a marked increase in crustal thickness from ∼30 to 40 km or greater (Gilbert, 2012), a similarly abrupt decrease in heat flow (Lachenbruch, 1978; Davies, 2013) (47 ± 16 mWm^{-2} to 83 ± 21 mWm^{-2}), and reduction in crustal extension rates of ∼2–3 mm/yr to virtually zero (Chang *et al.*, 2006; UNAVCO, 2020). The west-dipping normal fault that defines the western flank of the Wasatch mountains is recognized to accommodate the larger share of the extension (Schwartz and Coppersmith, 1984; DuRoss *et al.*, 2016). On the basis of structural analysis of seismic reflection profiles and geodetic observation, it has been interpreted that the Wasatch range bounding fault is listric rather than planar at depth (Smith and Bruhn, 1984; Mohapatra and Johnson, 1998; Velasco *et al.*, 2010), though the idea has yet to be tested with the occurrence of a large sur-face-rupturing earthquake along the Wasatch. The M_w 5.7 Magna epicenter and aftershocks are located within the Intermountain Seismic belt and along the Wasatch range bounding fault.

The region north of the east Snake River Plain also displays basin and range topography and normal faults distinguishable from those to the south by their northwesterly strike (light blue faults in Fig. 1). The zone of faults and associated seismicity has been labeled the Centennial Tectonic belt, following the study of Stickney and Bartholomew (1987). The Trans-Challis fault system (TCFS) consists of northeast-trending faults and erup-tive centers that correlate to and may provide structural control to the northwest extent of the major northwest ranges, basins, and normal faults that compose the area (Bennett, 1986). Instrumentally recorded seismicity within the belt is generally sparse and distributed (Fig. 1) except for distinct concentra-tions of seismicity at its margin in the vicinity of the 1959 M_w 7.3 Hebgen Lake normal-fault surface rupture (Witkind *et al.*, 1962), the Yellowstone Plateau, and what are the after-shock distributions of the Stanley and large normal 1983 M_w 6.9 Borah Peak earthquakes (Richins *et al.*, 1987). The east Snake River Plain is located along a time-transgressive belt of silicic and caldera-forming volcanism that commenced within the Owyhee Plateau ∼14–12 Ma and migrated northeastward to reach the Yellowstone Plateau about 2 Ma, where volcanic

processes remain active today (Pierce and Morgan, 1992). The time-transgressive sequence of volcanism is now generally attributed to migration of the North American continent over a mantle plume now commonly referred to as the Yellowstone "hot spot" (Morgan, 1972). Subsequent Quaternary eruptions of basalt flows are responsible for the smooth surface that marks the east Snake River Plain (Fig. 1 and Kuntz *et al.*, 1992). The Centennial Tectonic belt overall has been interpreted to share a similar structural style and history of development to that of the broader Basin and Range province to the south (Reynolds, 1979; Crone *et al.*, 1987), though near its margin with the Snake River Plain, volcanic processes associated with the passing of the Yellowstone Hot Spot are recognized to have modified or influenced the evolution of slip on major range bounding faults and current seismicity within the belt (e.g., Smith and Sbar, 1974; Scott *et al.*, 1985; Stickney and Bartholomew, 1987; Anders *et al.*, 1989; Pierce and Morgan, 1992; McQuarrie and Rodgers, 1998). The M_w 6.5 Stanley earthquake occurred near the western limit of clear basin and range physiography, extended north of the TCFS, and was located >100 km from the margin of the Snake River Plain.

The Earthquakes
18 March 2020 M_w 5.7 Magna event
In framework of regional seismicity. The location of the Magna event is labeled and shown by white dots within the dashed polygon that encompasses the Wasatch Mountains in Figure 1. The noticeable increase in the recorded number of events per year during 1975–1980 followed a significant modernization of the Utah seismic network (Arabasz, 1979) (Fig. 2a). Seismicity here also shows most events occurring at midcrustal depths of 5–10 km (Fig. 2b,c), with a lesser number of events located at depths reaching to 20–25 km. The log of the cumulative number of events (N) greater than or equal to magnitude M per year since 1980 is plotted in Figure 2d. The observations are characterized by a b-value of 1.1 when fit to the Gutenberg–Richter relationship $\log N/\mathrm{yr} = a - bM$. Assuming 34 yr of recording is sufficiently representative of longer-term rates of seismicity, the curve fit predicts the expectation of an **M** 6.5 or greater earthquake every ~184 yr. In this regard and to similar prior analyses (e.g., Working Group on Utah Earthquake Probabilities [WGUEP], 2016), the lack of any **M** 6.5 or greater earthquakes in the historical record can reasonably be expected. Similarly, the plot indicates that events equal to or greater than the **M** 5.7 event may be expected every 25 yr or so.

Mainshock and aftershocks. Aftershocks from the ANSS catalog are confined to depths between 5 and 12 km (Fig. 3a) with the majority between 8 and 10 km (Fig. 3c). The mainshock hypocenter determined with travel time is ~12 km and at the lowest depth of the aftershock distribution (Fig. 3a,c). The plot of aftershocks as a function of depth along a 50°

azimuth (trend of majority of faults along Wasatch) suggests an inclination and thus dip of the fault plane to the southwest, consistent with displacement on the near north-striking nodal plane of the focal mechanism for the event shown in Figure 1. The rupture appears to have propagated up-dip from the hypocenter. The event occurred in the densest portion of the Utah Regional Seismic Network (Pankow *et al.*, 2020) and the depth uncertainties attached to the event locations average <0.7 km. The most recent report of Pang *et al.* (2020) that further incorporates seismograms collected from instruments deployed soon after the earthquake, regional moment tensor inversion of broadband waveforms, and template-based detection of aftershocks brings yet significantly greater resolution in defining event locations and the geometry of the causative fault. They place the centroid depth at 9 km below the surface and resolve coseismic slip was oblique-normal, limited to depths of ~9–12 km, and on a shallow 30°–35° west-dipping fault, consistent with the idea that the Wasatch range front fault is listric at depth.

More than 100 aftershocks of **M** 2 and greater occurred in the day following the mainshock (Fig. 3b,d), and then rapidly and exponentially decayed to less than an aftershock per day a week following the event. The decay rate is formalized with a curve fit in the form of the modified Omori Law of Utsu (1961) with a p-value of 0.74 in Figure 3d. The b-value of the aftershock distribution when plotted in the form of the Gutenberg–Richter distribution (Fig. 3e) is 0.71, less than the value of 1.1 observed for the entirety of the region (Fig. 2e).

In framework of active faults, instrumentally recorded seismicity, and geodetic velocity field. The aftershock distribution of the Magna earthquake is plotted in the context of the distribution of nearby active faults, the geodetic velocity field, and seismicity in Figure 4. The historical and instrumental record along the Wasatch, though absent of major surface rupture earthquakes, has identified a number of moderate-size events prior to the Magna earthquake that have gained the attention of analysts and are noted in Figures 1 and 4. The 1884 **M** 6.3 Bear Lake earthquake is the earliest (Fig. 1). Evans *et al.* (2003) integrate felt reports with geologic observation to interpret the event occurred on an east-dipping normal fault antithetic to a major west-dipping normal fault. The M_w 1934 Hansel Valley earthquake was accompanied by upward of 5 km of generally north to northeast-striking and commonly en échelon ground cracks (Bodle, 1934; Shenon, 1936) that most recently have been correlated with seismic profiling to correlate spatially with subsurface offsets in Quaternary deposits (Bruno *et al.*, 2017). The analysis of Doser (1989) of P waveforms for the event places the event M_w at 6.6 and suggests the earthquake produced largely left-slip on a northeasterly striking fault plane, consistent with east–west tension. The nearby 1962 Cache Valley earthquake was subjected to similar waveform analysis, assigned a moment
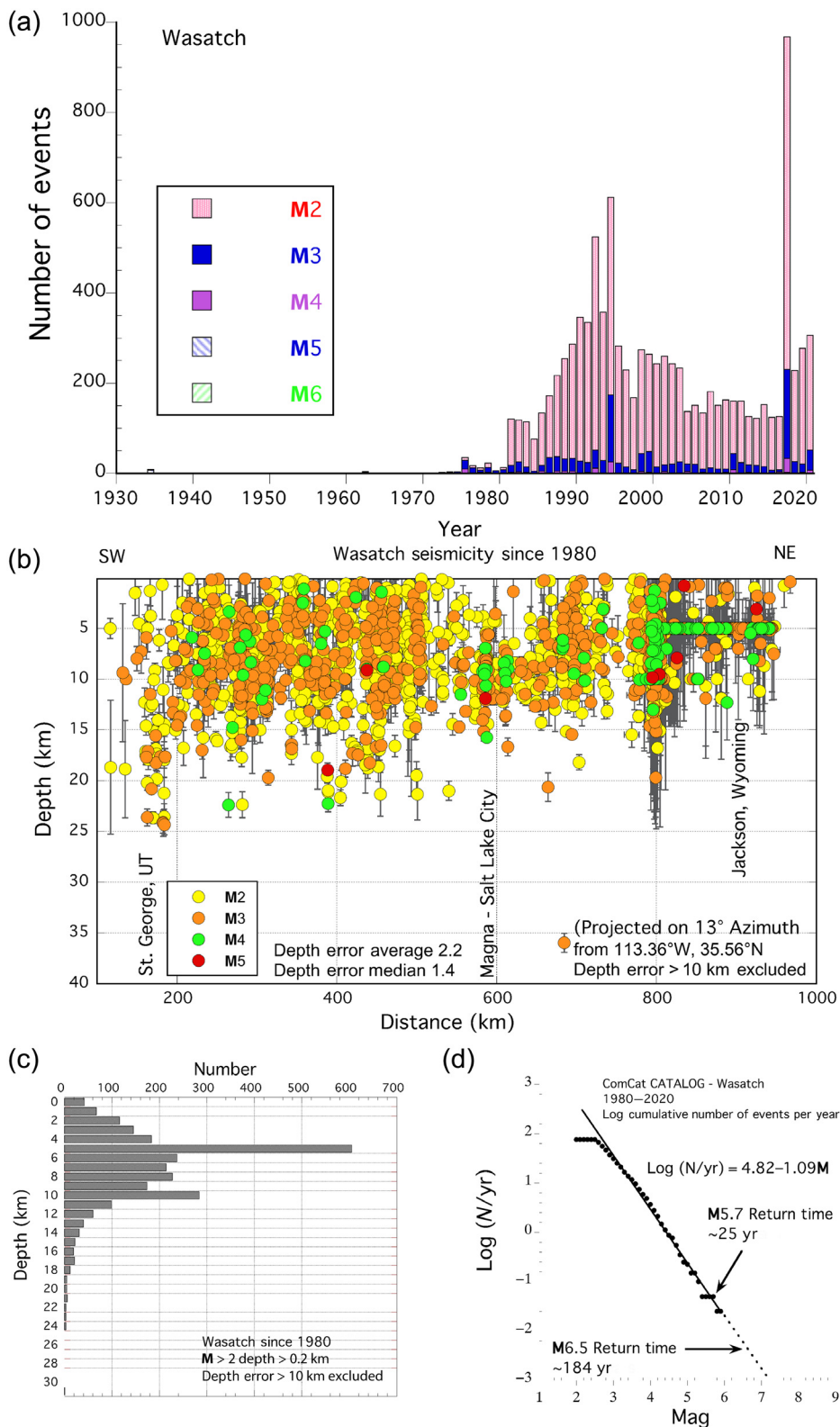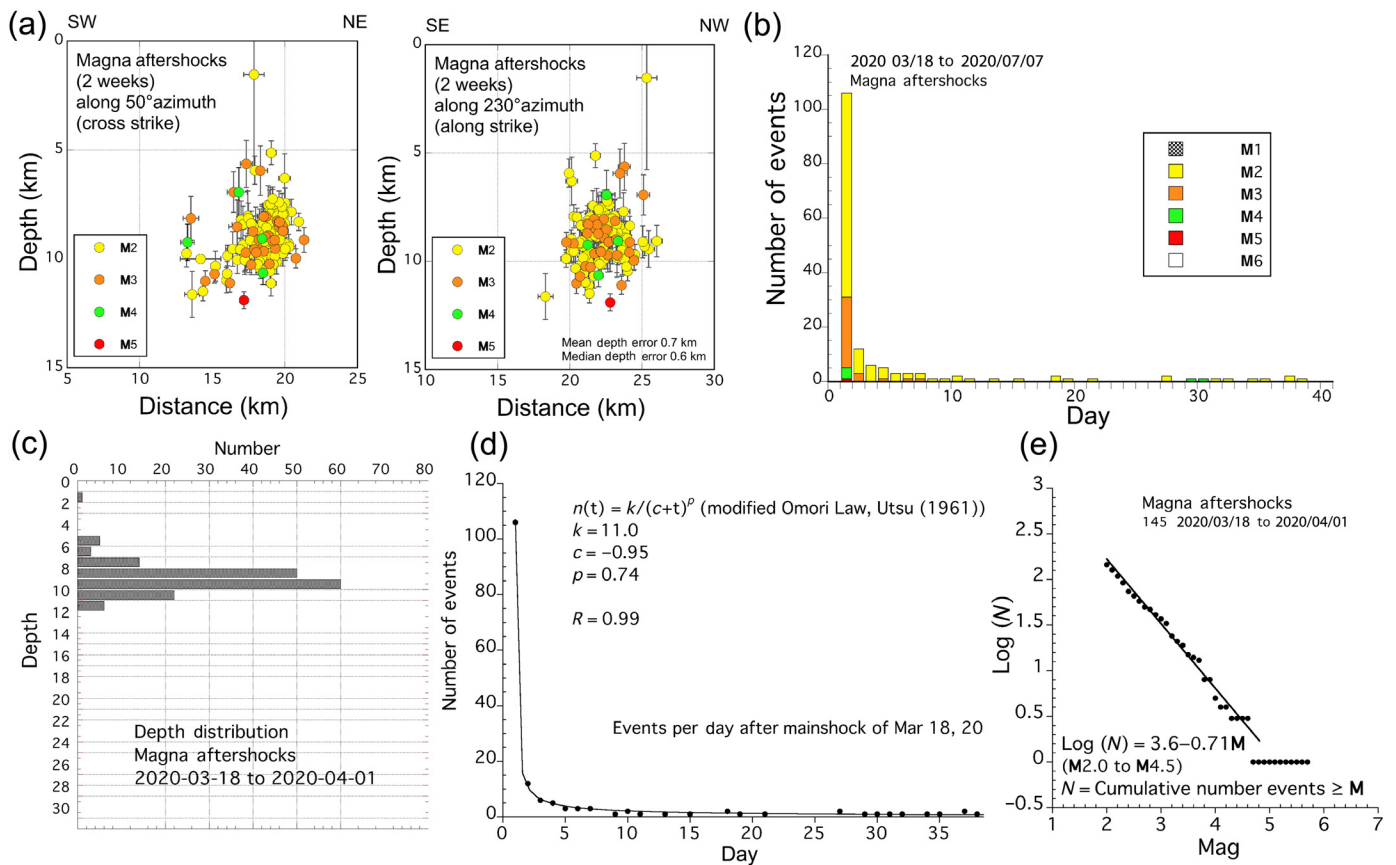
Figure 2. Characteristics of instrumental record of seismicity along Wasatch range. (a) Number of events per year. (b) Hypocentral depths versus distance projected along 13° azimuth. (c) Number of events versus depth. (d) Log of cumulative events per year versus magnitude annotated to show average period of time between selected moderate and large magnitude earthquakes. Sampled area outlined by dashed polygon encompassing Wasatch range in Figure 1. The color version of this figure is available only in the electronic edition.

magnitude M_w 5.6, and attributed to slip on a northeast-striking oblique normal fault (Westaway and Smith, 1989). Immediately to the north first-motion study and waveform analysis of the 1975 Pocatello Valley earthquake show the M_w 6.1 event was produced by normal displacement on a northerly dipping fault plane. The Pocatello event was accompanied by ground fractures but apparently an absence of primary surface rupture on the causative fault (Coffman and Stover, 1975; Arabasz *et al.*, 1981). The most recent 2017 M_w 5.3 Sulphur Peak mainshock similarly exhibits normal displacement on a northerly striking fault plane and distinguished by an energetic aftershock sequence attributed to aseismic afterslip (Koper *et al.*, 2018). In sum, each of the events exhibited focal depths less than 10 km and produced slip consistent with east–west crustal extension. When viewing the Magna event location in context of the entire record of instrumentally recorded events, small events have occurred in the vicinity of the Magna earthquake since 1972 though the number is not particularly elevated in comparison to that observed in locations elsewhere in the region.

The number of paleoearthquake studies of active faults along the Wasatch range is numerous. They have been synthesized in a number of studies addressing characteristics of earthquake behavior (e.g., Schwartz and Coppersmith, 1984; Machette *et al.*, 1991; DuRoss *et al.*, 2016). The consensus report

Figure 3. Magna earthquake aftershock characteristics. (a) Aftershocks shown in Figures 1 and 4 reprojected as function of depth along azimuths approximately parallel (∼330°) and perpendicular (∼70°) to the trend of major adjacent active faults. Distances measured from −111.938° W, 40.576° N and −112.229° W, 40.645° N, respectively. Average and median depth errors are 0.66 km and 0.59 km, respectively. (b) Histogram of number of events of each magnitude per day after mainshock. (c) Number of aftershocks as function of depth. (d) Total number of aftershocks per day with damped least-squares fit (Marquardt, 1963) to modified Omori Law relationship. *R* is Pearson correlation coefficient. (e) Cumulative number (*N*) of aftershocks as function of magnitude **M**. The color version of this figure is available only in the electronic edition.

of Lund (2005) also considers other major faults mapped adjacent to the range front. The brief accounting of fault characteristics (slip rates and recurrence times) that follows is, unless otherwise noted, derived from this latter report. Active faults in the region encompassed by Figure 4 are invariably of normal mechanism and north striking, oriented to accommodate east–west crustal extension. The geodetic velocity field in like manner shows 2–3 mm/yr of extension occurring across the range front today (Fig. 4 and Chang *et al.*, 2006; Kreemer *et al.*, 2010). The most prominent and continuous active fault in the vicinity of the Magna event is the west-dipping normal fault that runs along the western front of the Wasatch range. Pang *et al.* (2020) utilize this spatial relationship in conjunction with the depth and low-angle normal mechanism of Magna aftershocks to interpret that the Wasatch range front fault here is listric. Exhumation of the Wasatch range front and range front faulting commenced ∼11 Ma (Kowallis *et al.*, 1990; Armstrong *et al.*, 2003). Preferred vertical Holocene slip rates reported for the main range bounding fault are generally on the order of 1.1–1.4 mm/yr (Fig. 4). Discussions today generally divide the range front fault into a number of named sections or segments, each separated by geometrical complexities in fault strike such as steps and bends and defined by a unique paleoseismic history. From north to south, these include the Brigham City, Weber, Salt Lake City, Provo, Nephi, and Levan fault segments. Faults subparallel and west of the main range front fault system include the East Great Salt Lake, Oquirrh, Utah Lake, and West Valley faults. Where reported, best estimates of the average return time of surface rupture earthquakes on the faults and fault segments are generally in the range of 1–2 k.y. along the range front and greater for those faults to the west (Fig. 4). Displacements registered in individual events are generally 1–2 m or more (DuRoss *et al.*, 2016) and from comparison to historically observed earthquakes are reasonably considered the result of earthquakes of **M** 6.5–7 and greater (e.g., Wells and Coppersmith, 1994).
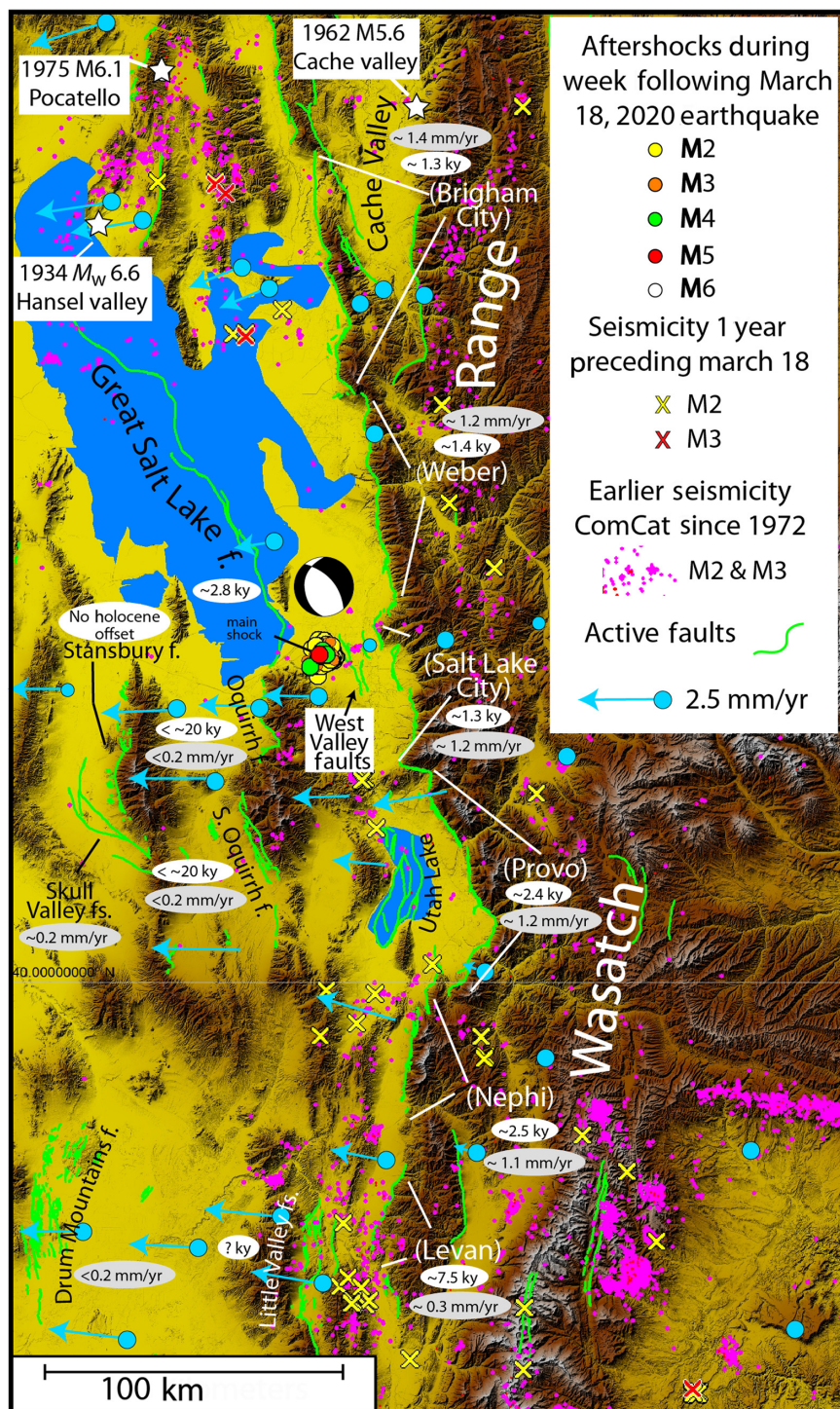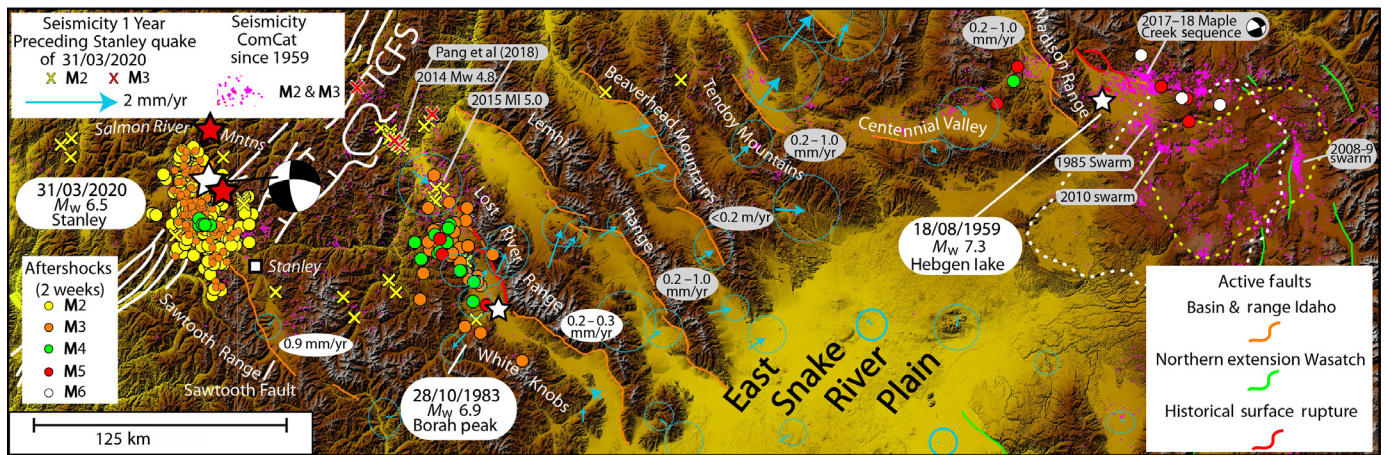
Figure 4. Epicenters of mainshock and aftershocks of 18 March 2020 M_W 5.7 Magna earthquake on physiographic map showing location of major surrounding active faults, the geodetic velocity field (blue arrows) and epicenters of earthquakes registered in year preceding the mainshock. Names of sections of the major normal fault that bounds the western edge of the Wasatch range (white, in parentheses) are taken from the USGS Fault and Fold Database (USGS, 2020b). Focal mechanism of mainshock from ANSS ComCat (USGS, 2020a). Orientation of Magna event nodal planes are strike 182°, dip 34°, rake −52°, and strike 319° dip 64°, rake −112°. Average mid- to late-Holocene slip rates and average recurrence intervals between surface rupture earthquakes are in gray and white ovals, respectively. Values along Wasatch range front, the Great Salt Lake fault, and Oquirrh faults are best estimates reported by Lund (2005). Geodetic velocity vectors (light blue) copied from UNAVCO (2020) and with respect to stable North America reference frame. The color version of this figure is available only in the electronic edition.

Seismicity preceding the mainshock and comparison of rates of large earthquakes observed geologically and from modern seismicity. Epicenters of earthquakes in the year preceding the earthquake are shown by crosses in Figure 4. The epicenters are widely distributed. No measurable foreshocks preceded the Magna earthquake. The paleoearthquake record makes clear that the Magna earthquake is preceded by numerous prehistoric surface ruptures on surrounding faults. An accounting of the paleoearthquake reported by Lund et al. (2005) for the faults shown in Figure 4 shows 25 surface rupture earthquakes occurring in the preceding 7000 yr. DuRoss et al. (2016) more recently give a similar accounting of ∼24 events in the last 6–7 ka on the Wasatch range front. Notwithstanding uncertainties arising from a possibly incomplete paleoseismic record, the potential of large earthquakes occurring on unmapped faults, and the possibility that some paleoearthquakes along the Wasatch range front actually occurred at the same time, the occurrence of 25 surface ruptures during 7000 yr equates on an average return time of **M** 6.5 and greater earthquakes on the order of 280 yr, assuming that surface rupture earthquakes register magnitudes of **M** 6.5 and greater. This value of average return time of events in the region is somewhat greater than the ∼184 yr implied by rates of instrumentally recorded seismicity shown in Figure 2d.

Figure 5. Epicenters of mainshocks (white stars) and aftershocks in two weeks following each of the 31 March 2020 M_W 6.5 Stanley, Idaho, the 28 October 1983 Borah Peak, and 18 August 1959 Hebgen Lake earthquakes on physiographic map showing location of major surrounding active faults (orange). Red stars are **M** > 6 earthquakes of 1944 and 1945 reported by Dewey (1987). Portions of faults experiencing historical surface rupture are red. Epicenters of all events in ComCat since 1959 shown as magenta dots and those registered in the year before the Stanley earthquake denoted by crosses. Focal mechanism of Stanley mainshock from ANSS ComCat (USGS, 2020a). The focal mechanism of the Stanley event is described by nodal planes with strike 269°, dip 67°, rake −163°, and strike 172°, dip 74°, rake −24°, respectively, and the horizontal projection of a *T* axis that is oriented at 222°. Blue arrows are geodetic displacement rate arrows and 70% confidence ellipses from Payne et al. (2013) plotted with respect to a stable Snake River Plain reference frame. Values in white ovals are slip rates of adjacent faults reported by investigators cited in the In Framework of Active Faults and Geodesy section and those in gray ovals from the USGS Fault and Fold Database (USGS, 2020b). White and yellow dotted lines approximate boundaries of 2.1 and 0.64 Ma Yellowstone Calderas. The 1985, 2008–2009, and 2010 earthquake swarms within Caldera are documented in Waite and Smith (2002), Farrell et al. (2010), and Shelly et al. (2013), respectively. TCFS, Trans-Challis Fault System from Bennett (1986). The color version of this figure is available only in the electronic edition.

31 March 2020 M_W 6.5 Stanley, Idaho, event

In framework of regional seismicity. Event aftershocks place the Stanley earthquake north of the Snake River Plain (Figs. 1 and 5). Seismicity within the dashed polygon shown in Figure 1 that encompasses the aftershocks is plotted as the number of recorded earthquakes per year in Figure 6. The rapid increase in number of recorded events per year in the 1970s correlates with the initiation and development of the Idaho National Lab seismic monitoring program (Payne *et al.*, 2005). The relative increase in the number of **M** 2 events with time, particularly around 2014, likely reflects an improvement of the regional seismic network and capability to detect relatively smaller earthquakes. Seismicity is largely concentrated at depths <15 km, and virtually absent below depths of 20 km (Fig. 6b,c). The log of the number of events per year since 1975 is plotted in Figure 6d. That the network over this time period is only complete for **M** > 3 events is indicated by the lessening of the slope below **M** 3. Similarly, the lessening in slope at **M** ≳ 4.7 likely reflects the short duration of the catalog as compared with the actual return times of earthquakes greater than this magnitude. The best-fitting curve of the form $\log N = a − b\text{M}$ displays a slope (*b*-value) of 1.2 constructed with events only between **M** 3.0 and 4.7. Extrapolation of the curve fit yields the expectation of an **M** 6.0 or greater earthquake every ∼77 yr, in contrast to the numerous **M** > 6 earthquakes that have occurred since the 1940s. It may reasonably be suggested that the mismatch in significant part arises from the shorter and less complete instrumental record of seismicity for this area.

Mainshock and aftershocks. Recognizing that location uncertainties particularly with depth is significantly greater here than in the vicinity of the other two earthquakes, aftershocks during the two weeks after the mainshock are mostly confined to depths between 5 and 15 km (Fig. 7a) with the mainshock hypocenter at ∼12 km. The general alignment of aftershocks in map view is northerly (Fig. 5) and the plot of aftershocks as a function of depth along a 75° azimuth (left panel of Fig. 7a) appears to delineate the vertical plane. The two

observations taken together suggest that displacement responsible for the earthquake occurred on the north-striking left-lateral nodal plane of the mainshock focal mechanism (Fig. 5). As with the Magna earthquake, significantly greater resolution of the fault architecture will arise with further analysis of arrival time and waveform data collected with instruments deployed soon after the earthquake (e.g., Liberty *et al.*, 2021).

Aftershocks of **M** 2 and greater during the day following the mainshock surpassed 100 (Fig. 7b). The rate subsequently decreased in exponential fashion to an average of ∼10 per day a month after the mainshock, and this rate held steady for an
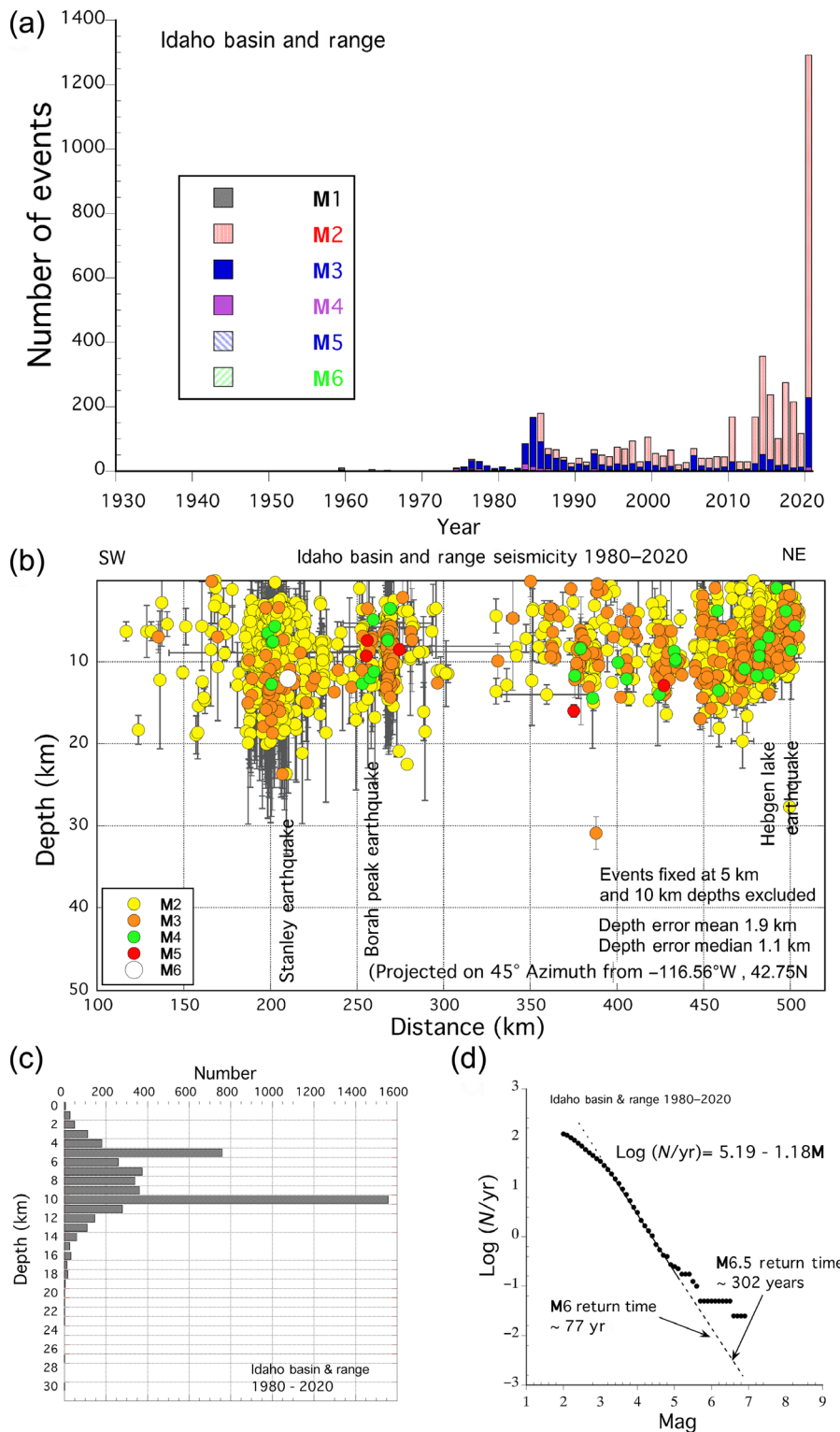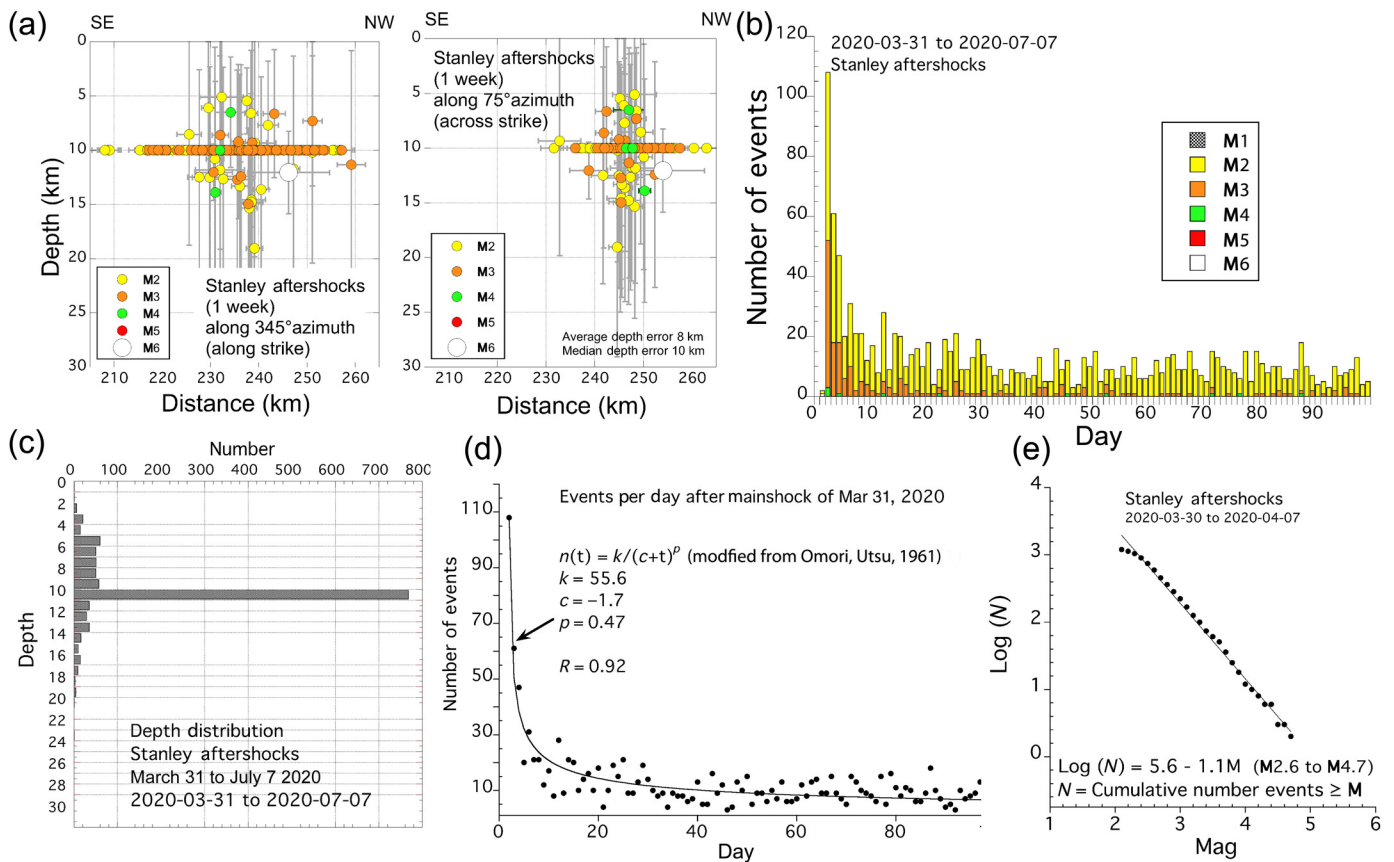
Figure 6. Characteristics of instrumental record of seismicity within Idaho Basin and Range (dashed polygon outlining Centennial Tectonic belt in Fig. 1b). (a) Number of events per year. (b) Hypocentral depths versus distance projected along 45° azimuth. (c) Number of events versus depth. (d) Log of cumulative events per year versus magnitude annotated to show average period of time between selected moderate and large magnitude earthquakes. Sampled area outlined by dashed polygon in Figure 1. The color version of this figure is available only in the electronic edition.

additional two months. Curves of standard exponential form and the modified Omori Law of Utsu (1961) are fit to the observed number of events per day in Figure 7d. Approximations of the aftershock decay rate are provided with the modified Omori Law with a p-value of ~ 0.5. The b-value of the aftershock distribution when plotted in the form of the Gutenberg–Richter distribution is 1.1 (Fig. 7e), as compared with the value of 1.2 observed for the entirety of the region (Fig. 6d).

In framework of active faults and geodesy. The basin and range structure north of the Snake River Plain is the result of displacement on a set of northwest-striking, primarily normal faults distributed between about the Madison range on the east and Sawtooth range to the west (Fig. 5). Neotectonic studies bearing on fault-slip rates and paleoearthquake histories are few in comparison to the Wasatch Range. Thackray et al. (2013) document several latest Pleistocene–Holocene displacements and a vertical slip rate of 0.9 mm/yr along the Sawtooth fault that extends southward from the area of Stanley aftershocks, and further postulate that active faulting may have migrated northward along the fault during Pleistocene time. Late Pleistocene faulting along the Lost River Range is demonstrated with surface ruptures that accompanied the 1983 Borah Peak earthquake. Most topical studies concur faulting previously occurred along the fault from 15 ka (Haller and Wheeler, 2020). Fault

Figure 7. Stanley earthquake aftershock characteristics.
(a) Aftershocks shown in Figure 5 projected as function of depth along northwest (345°) and northeast (~75°) azimuths. Distances measured from 114.478° W, 42.296° N and –118.179° W, 43.826° N, respectively. Average and median depth errors are 8 and 10 km, respectively. Average and horizontal location errors are 2.6 and 2.4 km, respectively. (b) Histogram of number of events of each magnitude per day after mainshock. (c) Number of aftershocks as function of depth. Large spike at 10 km depth is artifact of assignment of this depth to events for which depth constraints are poor and absent. (d) Total number of aftershocks per day with damped least-squares fit (Marquardt, 1963) to modified Omori Law relationship. *R* is Pearson correlation coefficient. (e) Cumulative number (*N*) of aftershocks as function of magnitude **M**. The color version of this figure is available only in the electronic edition.

morphology and displaced alluvial surfaces provide the basis on which Hanks and Schwartz (1987) and Scott *et al.* (1985) estimate that the portion of the fault that broke in 1983 slips at ∼0.2–0.3 mm/yr. Studies documenting fault-slip rates and paleoearthquake histories are largely absent from professional publications for the remaining normal faults shown in Figure 5. Compilers of the USGS Fault and Fold Database, which also draws upon unpublished geologic reports, place the slip rates of the remaining faults broadly between 0.2 and 1.0 mm/yr. Values within the lower end of this range are suggested by Pierce and Morgan (1992) analogous compilation and assessment of offsets across the same faults.

Global Positioning System derived surface velocities of Payne *et al.* (2013) for the period of 1994–2010 are reproduced in Figure 5. The velocities are plotted with respect to a stable Snake River Plain reference frame. The subparallel trend and increasing size of the vectors from southeast to northwest indicate ongoing extension perpendicular to the trend of the major normal faults is on the order of ∼1 mm/yr. If representative of the long term, the geodetic rate would imply that the geologic fault-slip rates fall at the lower end of the 0.2–1.0 mm/yr range reported by the USGS. The general increase in velocities along transects extending northeast from Snake River Plain is additionally interpreted by Payne *et al.* (2013) to indicate the area is experiencing right-lateral shear at 0.3–1.5 mm/yr. The velocity field shows transtension in a manner like that observed in the Walker Lane (Fig. 1). In this instance, it appears that

normal faulting is the dominant mode of strain release in contrast to strike-slip faulting in much of the Walker Lane. The northwest-trending, left-stepping, en échelon pattern of faulting along the east-striking Centennial fault reported by Petrik (2008), cited by Payne *et al.* (2013), and observed in seismic reflection profiles by Bruno *et al.* (2019) are consistent with the interpreted right-lateral shear.

An intuitive explanation of the location and mechanism of the Stanley event is not easily gained within this framework of active faulting and geodetic deformation. The major faults in this region are primarily normal faults. The Stanley event

occurred on none of these faults and is the result of slip on a north-striking left-lateral fault. Unlike other mapped faults of the area, the Stanley earthquake is within rugged terrain devoid of an adjacent basin and appears to cross and extend north of the TCFS. One may speculate that the event in some manner reflects the northward progression of Pleistocene activity on the Sawtooth fault suggested in the Thackray *et al.* (2013) study. The main consistency of the Stanley earthquake with the major mapped faults of the area is that the focal mechanism shows it to share a similar direction of crustal extension (*T* axis) that accompanies normal displacement on other major faults in the area.

Seismicity preceding the mainshock. The 18 August 1959 M_w 7.3 Hebgen Lake and 28 October 1983 M_w 6.9 Borah Peak earthquakes are the largest historical earthquakes in the region to precede the Stanley earthquake (Fig. 5). Each today is among the best examples of earthquakes that produced surface rupture along range bounding normal faults, and among the largest earthquakes that have produced surface rupture within continents. The Hebgen Lake event is located immediate north of the Yellowstone Caldera. The abundant seismicity within and along the margins of the caldera consists predominantly of swarms of earthquakes generally attributed to stress perturbations associated with the migration of magmatic or hydrothermal fluids or aseismic slip and fluid pressure variations. The 2017–2018 Maple Creek sequence of earthquakes that occurred just outside the caldera consisted of some 3000 events and are interpreted by Pang *et al.* (2019) in part to be long-lived aftershocks of the 1959 Hebgen Lake event. Between the Hebgen and Borah Peak ruptures, instrumentally recorded seismicity is broadly distributed and at a low rate of activity. In the year prior to the Stanley earthquake, a significant number of **M** 2 and 3 events occurred immediately northwest of the Borah Peak surface rupture and aftershocks. These may be a further continuation of the 2014–2017 energetic sequence of small earthquakes that Pang *et al.* (2018) interprets as late aftershocks of the Borah Peak earthquake. It is difficult to attribute significance to the few **M** 2 earthquakes that occurred in the vicinity in the year preceding the mainshock. Felt reports (Bodle, 1946) and relocations (Dewey, 1987) of two **M** 6 earthquakes on the edges of the Stanley aftershock zone (red stars in Fig. 5) are evidence of prior and significant seismic activity near the Stanley quake. Dewey (1987) cautions that the relocated epicenters may be in error up to 40 km or more.

15 May 2020 M_w 6.5 Monte Cristo mountains event

In framework of regional seismicity. The aftershock distribution delineates the location of the event within the Walker Lane–Eastern California shear zone (white dots in Fig. 1). The number of recorded earthquakes per year within the dashed polygon encompassing Walker Lane–Eastern California shear zone is plotted in Figure 8a. The instrumental record of seismicity extends back to about 1930. The abrupt increase in number of events per year around 1975 in significant part reflects increased instrumentation accompanying establishment of the Nevada Seismological Laboratory in 1974 (Nevada Seismological Laboratory [NSL], 2020). Seismicity is largely concentrated at depths <15 km, and earthquakes below this depth are generally limited to smaller **M** 2 and 3 events (Fig. 8b,c). The change in the maximum depth of seismicity in Figure 8c at ~800 km correlates to the boundary between reporting areas of different seismic networks that contribute to the ComCat catalog, and so perhaps an artifact of analysis or compilation rather than reflecting a tectonic process. The cumulative number of events (*N*) greater than or equal to magnitude **M** per year (yr) since 1975 are plotted in Figure 8d and fit with a curve of the form of the Gutenberg–Richter relationship $\log(N/\text{yr}) = a - b\text{M}$. The curve displays a slope (*b*-value) of 0.96 and allows a general estimate that **M** 6.5 and greater earthquakes can be expected on average each ~12 yr.

Mainshock and aftershocks. Aftershocks during the week after the Monte Cristo mainshock are generally limited to depths <20 km (Fig. 9a) with the majority above ~15 km (Fig. 9c). The mainshock hypocenter is about 3 km, well above the depths at which most aftershocks occurred (Fig. 9a,c). In comparison, the centroid moment tensor depth is reported at ~9 km. Aftershocks of **M** 2 and greater averaged more than ~50 per day during the week after the mainshock (Fig. 9b, d), with the rate decaying exponentially over the course of 40 days to an average of ~10 aftershocks per day. The rate of decay is fit to the modified Omori Law of Utsu (1961) in Figure 9d. A *p*-value of the modified Omori Law curve that provides a reasonably good approximation of the decay is 0.76. The *b*-value of the aftershock distribution when plotted in the form of the Gutenberg–Richter distribution (Fig. 9d) is 0.83, in comparison to the value of 0.93 observed for the entirety of the Walker Lane–Eastern California shear zone.

In framework of active faults and historical surface rupture earthquakes. The aftershock distribution is shown in relation to the distribution of nearby active faults, the geodetic velocity field, and historical surface rupture earthquakes in Figure 10. Historically, the Monte Cristo event falls within a zone of large earthquakes that have produced surface rupture. Notable to the south are the right-lateral surface ruptures of the 1872 M_w 7.5 Owens Valley earthquake and the 1986 M_w 6.3 Chalfant Valley sequence of earthquakes. Immediately to the north are the right-lateral ruptures that occurred with the 1932 M_w 7.1 Cedar Mountain earthquake. The surface ruptures of the earthquakes of 1954 and 1915 farther to the north occurred on northeasterly trending normal faults within the Basin and Range. The northeasterly trend of aftershocks is near perpendicular to the strike of the
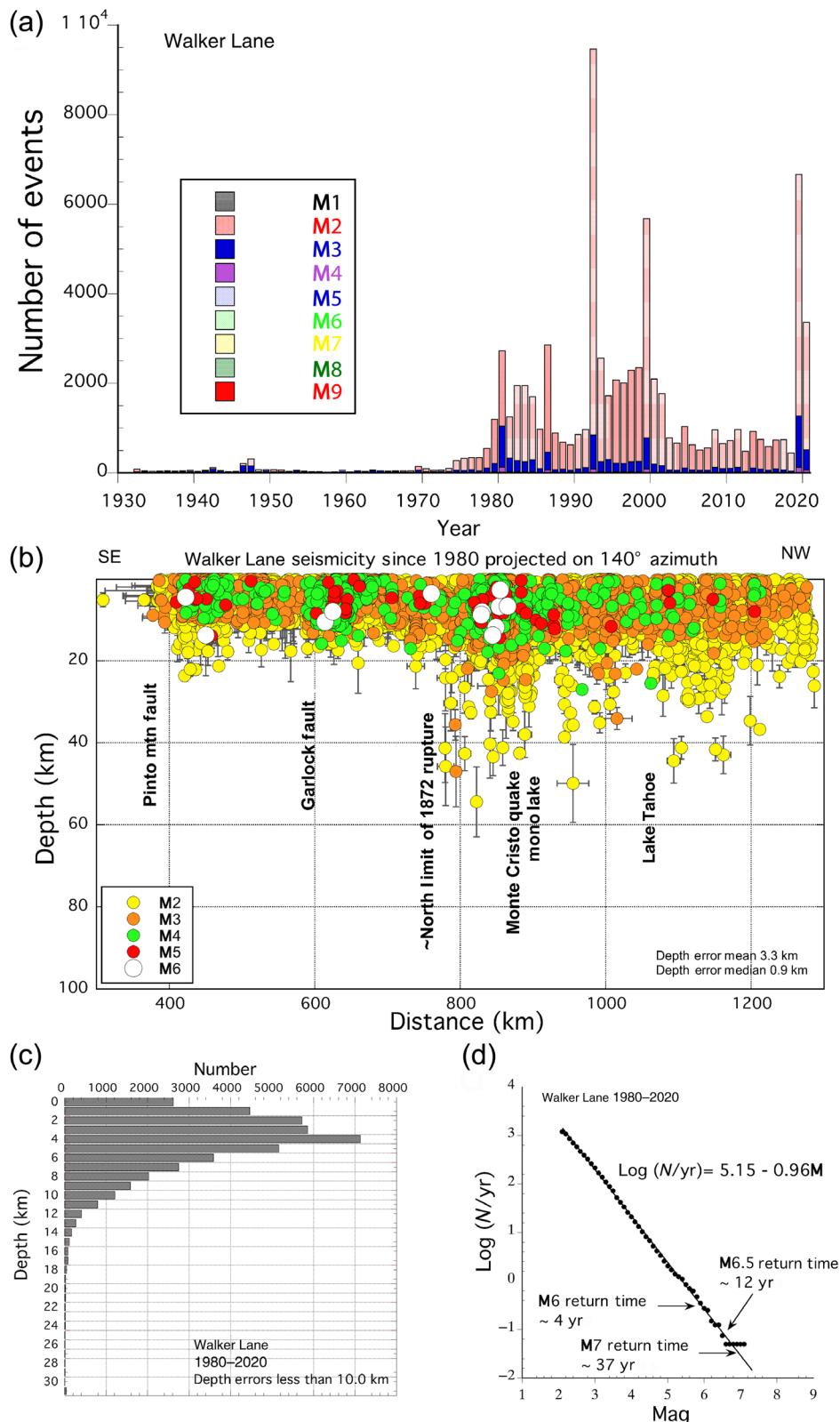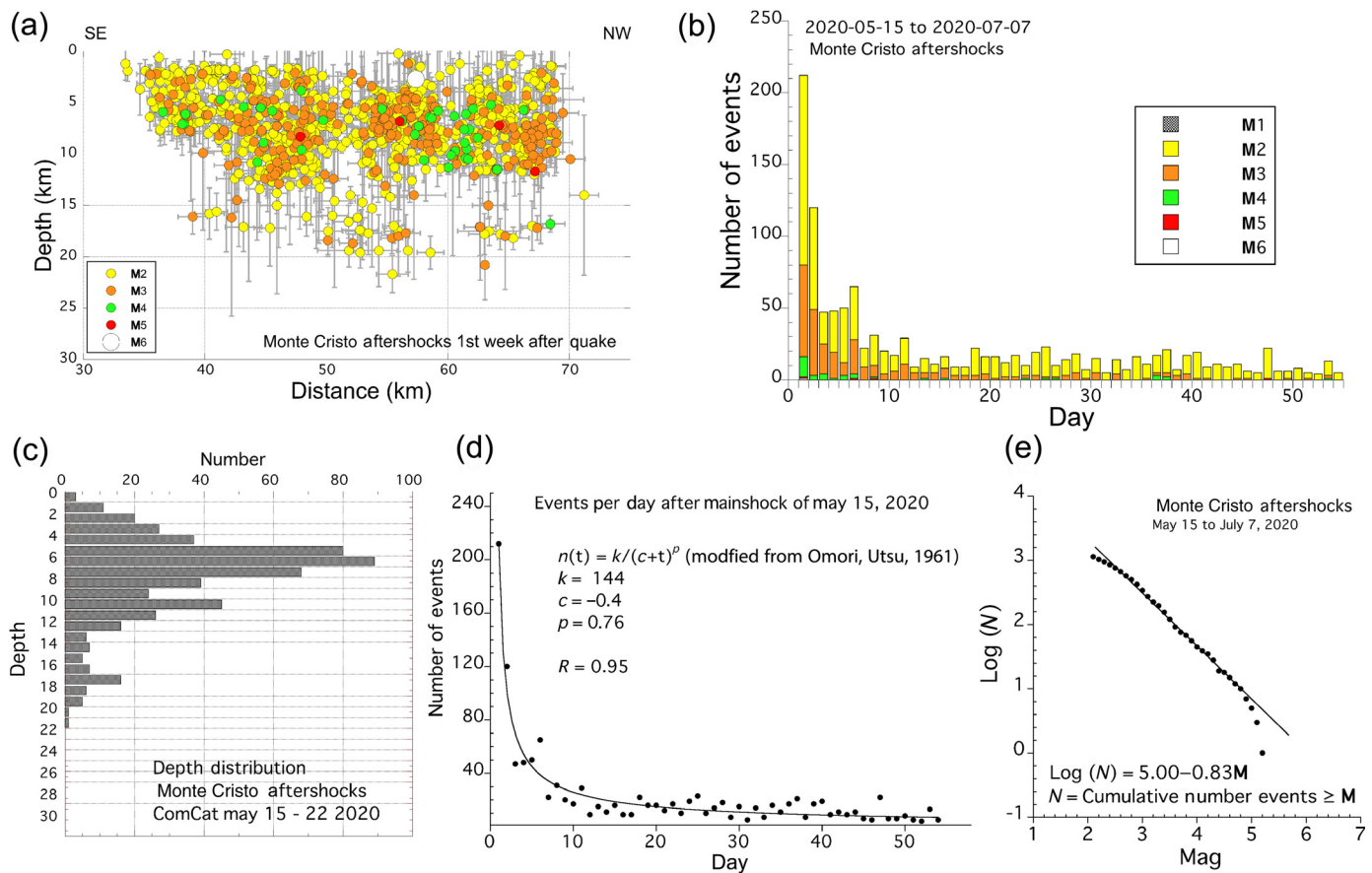
Figure 8. Characteristics of seismicity within dashed polygon of Figure 1 that encompasses the Walker Lane-Eastern California shear zone. (a) Number of events per year. (b) Seismicity projected as function of depth along 140° azimuth. (c) Number of earthquakes as function of depth. (d). Cumulative number (*N*/yr) of earthquakes per year as function of magnitude **M**. The color version of this figure is available only in the electronic edition.

historical right-lateral strike-slip surface ruptures, on strike with the left-lateral nodal plane of the mainshock focal mechanism, and within an abrupt and broad right-step between northwest-striking right-lateral faults to the north and south, respectively. The geodetic displacement field (blue arrows in Fig. 10) shows the area of the broad step is characterized by both northwest-directed, right-lateral shear and extension (arrows increase in size on both southwest and northwest transects across the area). Viewed more closely in Figure 11a, the trend of aftershocks aligns with the left-lateral Rattlesnake, Teels Marsh, and Coaldale faults, and directly along the eastward projection of the Candelaria fault, all of which displace late Pleistocene and younger deposits (Wesnousky, 2005b). The location of aftershocks and mechanism of the mainshock confirm at seismogenic depths that block rotations rather than extensional faulting take up deformation in this right-step of the Walker Lane fault system (Fig. 12). It is expected that more detail of fault architecture will ensue with further analysis of arrival time and waveform data collected with instruments deployed soon after the earthquake (Bormann *et al.*, 2021; Ruhl *et al.*, 2021).

Surface rupture attributed to the Monte Cristo earthquake is dominated by the occurrence of ground cracking and about 14 km of fault trace that exhibits left-lateral displacements no greater than ∼15 cm (Koehler *et al.*, 2021). The trace overlaps the eastern end of the previously mapped Candelaria fault,

Figure 9. Monte Cristo earthquake aftershock characteristics. (a) Aftershocks shown in Figures 1a and 10 projected as function of depth along 70° azimuth. Distance measured from −118.49° W 38.023° N. Average and median depth errors are 3 and 2 km, respectively. Both mean and median horizontal errors are 1.2 km. (b) Histogram of number of events of each magnitude per day after mainshock. (c) Number of aftershocks as function of depth. (d) Total number of aftershocks per day with damped least-squares fit (Marquardt, 1963) to modified Omori Law relationship. *R* is the Pearson correlation coefficient. (e) Cumulative number (*N*) of aftershocks as function of magnitude **M**. The color version of this figure is available only in the electronic edition.

and strikes northeasterly from that overlap and away from the more easterly trend of aftershocks (Fig. 11). The aftershocks of recent large surface ruptures in the region have generally correlated directly to or followed the causative fault trace (Richins *et al.*, 1987; Hauksson *et al.*, 2002; DuRoss *et al.*, 2020). The lack of alignment of the surface rupture trace with the aftershock distribution appears enigmatic.

Seismicity preceding the mainshock. Several small earthquakes occurred at the site of the future Monte Cristo epicenter in August 2019 and another on 12 March 2020 (Fig. 11b). Whereas the events may in hindsight be interpreted to have occurred in preparation of the Monte Cristo earthquake, numerous similar small earthquakes also occurred elsewhere in the area during this same time period. The largest concentration of seismicity during this period of time is associated with the aftershocks of an **M** 5.2 earthquake that occurred well to the west near Mono Lake on 4 April 2020. Aftershocks in this earthquake also trend to the northeast.

Summary

Most characteristics of these Intermountain West earthquakes are largely consistent with expectations arising from observations accumulated over the ~40 yr since the implementation and subsequent growth of seismic networks in the region. Each occurred within a zone of relatively elevated seismicity,

active faults that exhibit Holocene displacement, historically hosted large surface rupture earthquakes and, in these regards, could be anticipated (Fig. 1). The depth distributions of seismicity in the broader regions associated with each event (Figs. 2c, 6c, and 8c) nicely illustrate that most seismicity in the Intermountain West is confined to depths of 5–10 km where it is interpreted that crustal strength or shear resistance is greatest (e.g., Sibson, 1982), that the amount of seismicity diminishes in exponential fashion to near zero between 15 and 20 km primarily due to rheological change (brittle–ductile transition) that accompanies increase in crustal temperature with depth (e.g., Scholz, 1988), and similarly decreases in number upward to the surface from the maxima at midcrustal
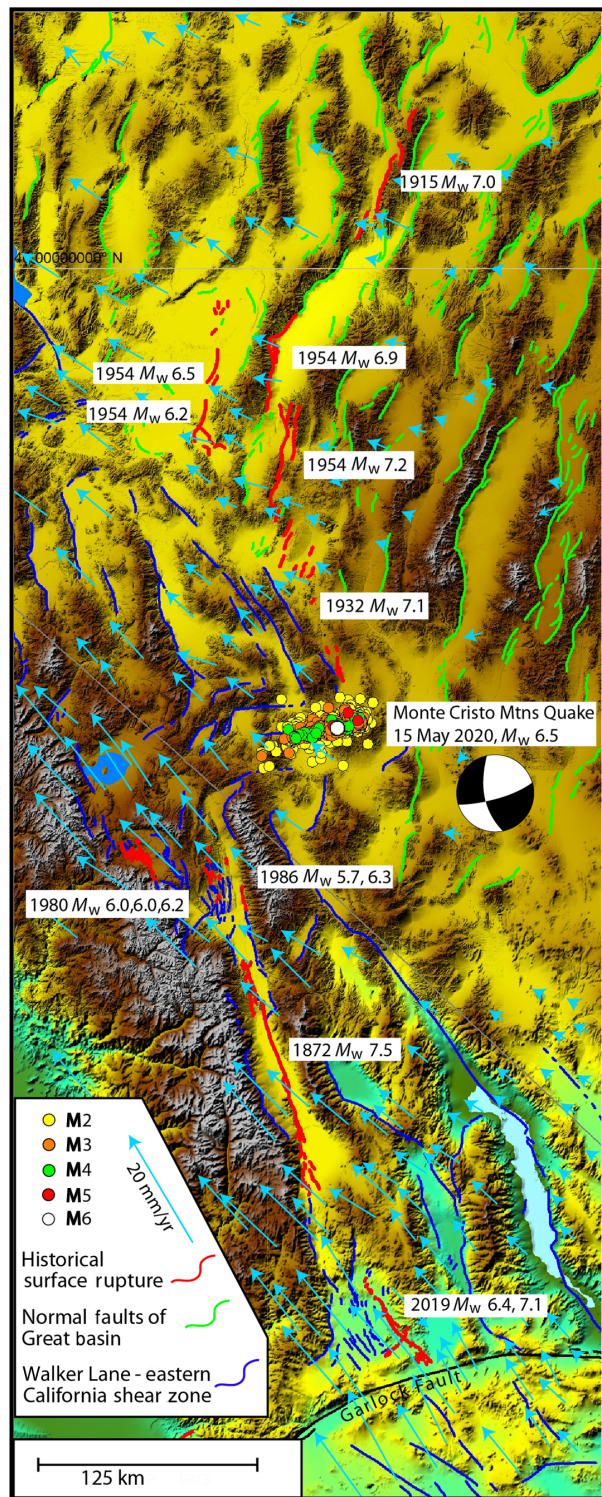
Figure 10. Epicenters of mainshock and aftershocks of 15 May 2020 M_W 6.5 Monte Cristo earthquake on physiographic map showing location of major surrounding active faults, where historical surface ruptures have occurred on those faults, and geodetic velocity field (blue arrows). Focal mechanism of mainshock from ANSS ComCat (USGS, 2020a). Geodetic vectors copied from Zeng and Shen (2016) with respect to stable North America reference frame. The color version of this figure is available only in the electronic edition.

depths, which has been attributed to velocity strengthening behavior of fault gouge at shallow crustal depths (Marone and Scholz, 1988). The Monte Cristo, Magna, and Stanley earthquake aftershocks follow the same pattern (Figs. 3c, 7c, and 9c). The brittle–ductile transition in each case falls well above the depth of Moho, which ranges from ∼30 to 40 km in the vicinity of each (Gilbert, 2012). As expected, the magnitude–frequency distribution of both the regions and the aftershock sequences are aptly described by the Gutenberg–Richter distribution. Whereas the b-values of the Gutenberg–Richter distribution vary between 0.7–1.1 and 1.0–1.2 for the aftershock sequences and encompassing regions, respectively, the analysis is insufficient to conclude the similarities and differences are significant.

Unfortunate though common, none of the mainshocks were preceded by a sequence of foreshocks to provide an obvious warning for preparation. Also as generally observed, the largest aftershock for each earthquake sequence is on the order of a magnitude unit less than the mainshock, the number of aftershocks correlates to the size of the mainshock, and the number of aftershocks each day subsequent to the mainshock decays exponentially subsequent to the mainshock. The p-value from the modified Omori law (Utsu, 1961) provides a measure of the aftershock decay rate that may be compared between earthquakes. The values obtained here for the Magna, Stanley, and Monte Cristo earthquakes are 0.71, 0.47, and 0 76, respectively (Figs. 3d, 7d, and 9d). Compilation of more than 200 similarly derived p-value estimates from more than 50 published papers reports p-values distributed between 0.6 and 2.5, with a median of 1.1 (Utsu *et al.*, 1995). It has been considered that the variability is related to various physical and tectonic factors such as structural heterogeneity, crustal stress, and temperature. Which if any of these is the most significant controlling factor is not to my knowledge established (Utsu *et al.*, 1995). To this puzzle then may be added the question why each p-value assessed here falls at the lower end of the spectrum of generally observed values.

Some aspects of the earthquakes do provide new tectonic insights or that perhaps appear contrary to expectation. The strike-slip mechanism of the Stanley earthquake stands in contrast to the zone of normal major range bounding faults and historical earthquakes to which it is adjacent, and it is the first relatively well instrumented rupture of an earthquake northward across the Trans-Challis fault zone (Fig. 5). The Pang *et al.* (2020) aftershock and moment-tensor analysis of the Magna earthquake gives further credence to the idea originally brought forth with seismic reflection and geodetic study (Smith and Bruhn, 1984; Velasco *et al.*, 2010) that the seismogenic Wasatch range bounding fault is listric, an idea that has yet to be confirmed by the occurrence of a large surface rupture event along the range front. The east-striking left-lateral mechanism Monte Cristo earthquake along the eastern margin of the Basin and Range might initially be viewed as contrary to expectation, though it can be viewed as expected from prior mapping
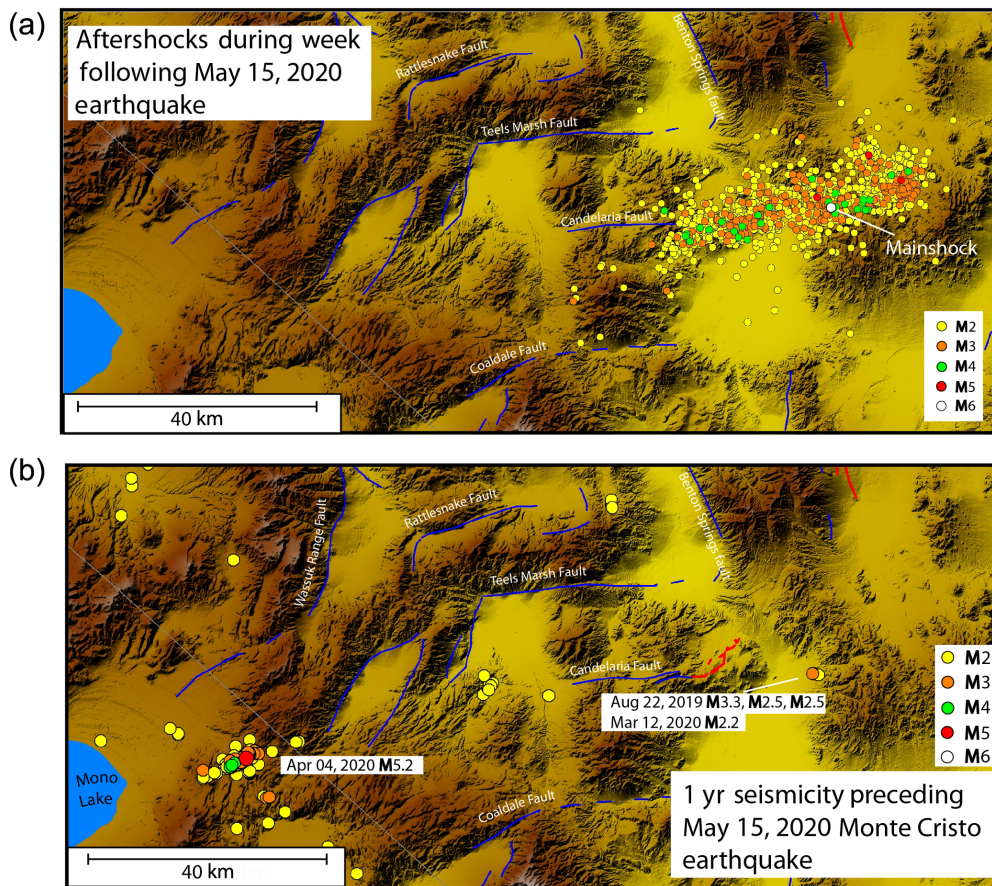
Figure 11. (a) Aftershock epicenters in week following the 15 May 2020 M_w 6.5 Monte Cristo mainshock. (b) Earthquake epicenters in year preceding mainshock and surface ruptures with left-lateral displacement extending northeastward from Candelaria fault (red lines) reported by Koehler et al. (2021). The color version of this figure is available only in the electronic edition.
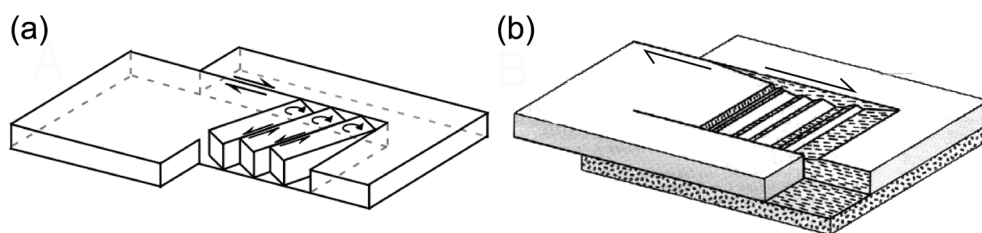

Figure 12. Aftershocks and focal mechanism of the Monte Cristo mainshock confirm that transfer of slip across the large right-step in the Walker Lane currently takes place as (a) rotation of crustal blocks rather than by (b) normal faults that commonly accompany extension in pull-apart basins.

of active faults in the area (Wesnousky, 2005b) and its location within the well-defined belt of transtensional shear that defines the Walker Lane (Fig. 10). Finally, the offset of a relatively well-defined zone of surface rupture to the well-defined trend of aftershocks during the Monte Cristo range earthquake seems unique in comparison to other observed strike-slip surface ruptures in the western United States (Richins et al., 1987; Hauksson et al., 2002; DuRoss et al., 2020).

Data and Resources

Seismological data in this article are sourced from Advanced National Seismic System (ANSS) Comprehensive Earthquake Catalog Event and Products (ComCat), available at https://earthquake.usgs.gov/data/comcat/. Locations of mapped active faults are adapted and modified from the U.S. Geological Survey Quaternary Fault and Fold Database website available at https://earthquakes.usgs.gov/hazards/qfaults. Digital elevation data used in construction of Figures 1, 4, 5, 10, and 11 accessed from the National Elevation Data Set hosted at https://www.usgs.gov/core-science-systems/national-geospatial-program/national-map and the global Shuttle Radar Topography Mission (SRTM) elevation model hosted at https://topex.ucsd.edu/WWW_html/srtm30_plus.html and described in Becker et al. (2009). All websites were last accessed in July 2020.

Acknowledgments

References

Anders, M. H., J. W. Geissman, L. A. Piety, and J. T. Sullivan (1989). Parabolic distribution of circumeastern Snake River Plain seismicity and latest Quaternary faulting—migratory pattern and association with the Yellowstone hotspot, *J. Geophys. Res.* **94,** no. B2, 1589–1621.

Arabasz, W. J. (1979). Historical review of earthquake-related studies and seismographic recording in Utah, *Special Publication of the University of Utah Seismograph Stations and the Department of Geology and Geophysics*, 33–56.

Arabasz, W. J., W. D. Richins, and C. J. Langer (1981). The Pocatello Valley (Idaho-Utah border) earthquake sequence of March to April 1975, *Bull. Seismol. Soc. Am.* **71,** no. 3, 803–826.

Armstrong, P. A., T. A. Ehlers, D. S. Chapman, K. A. Farley, and P. J. J. Kamp (2003). Exhumation of the central Wasatch Mountains, Utah: 1. Patterns and timing of exhumation deduced from low-temperature thermochronology data, *J. Geophys. Res.* **108,** no. B3, 17.

Becker, J. J., D. T. Sandwell, F. W. H. Smith, J. Braud, B. Binder, J. Depner, D. Fabre, J. Factor, S. Ingalls, S.-H. Kim, *et al.* (2009). Global bathymetry and elevation data at 30 arc seconds resolution: SRTM30_PLUS, *Mar. Geodes.* **32,** no. 4, 355–371.

Bennett, E. H. (1986). Relationship of the Trans-Challis Fault system in Central Idaho to Eocene and basin and range extensions, *Geology* **14,** no. 6, 481–484.

Bodle, R. R. (Editor) (1934). The Utah Earthquake, March 12, 1934, *Earthq. Notes (Seismol. Res. Lett.)* **V,** no. 4, 2–3.

Bodle, R. R. (Editor) (1946). *United States Earthquakes 1944, U.S. Coast Geodetic Surv. Serial No. 682*, 43 pp.

Bormann, J. M., W. C. Hammond, C. Kreemer, and G. Blewitt (2016). Accommodation of missing shear strain in the Central Walker Lane, western North America: Constraints from dense GPS measurements, *Earth Planet. Sci. Lett.* **440,** 169–177.

Bormann, J. M., E. A. Morton, K. D. Smith, G. M. Kent, W. S. Honjas, G. L. Plank, and M. C. Williams (2021). Nevada seismological laboratory rapid seismic monitoring deployment and data availability for the 2020 M6.5 Monte Cristo Range, Nevada earthquake sequence, *Seismol. Res. Lett.* this volume.

Bruno, P. P. G., C. Berti, and F. J. Pazzaglia (2019). Accommodation, slip inversion, and fault segmentation in a province-scale shear zone from high-resolution, densely spaced wide-aperture seismic profiling, Centennial Valley, MT, USA, *Sci. Rep.* **9,** 13.

Bruno, P. P. G., C. B. DuRoss, and S. Kokkalas (2017). High-resolution seismic profiling reveals faulting associated with the 1934 Ms 6.6 Hansel Valley earthquake (Utah, USA), *Geol. Soc. Am. Bull.* **129,** nos. 9/10, 1227–1240.

Chang, W. L., R. B. Smith, C. M. Meertens, and R. A. Harris (2006). Contemporary deformation of the Wasatch Fault, Utah, from GPS measurements with implications for interseismic fault behavior and earthquake hazard: Observations and kinematic analysis, *J. Geophys. Res.* **111,** no. B11, 19.

Coffman, J. L., and C. W. Stover (1975). United States Earthquakes, 1975, *U.S. Geol. Surv. Open-File Rept. 84-975*, 136 pp.

Cook, K. L., and R. B. Smith (1967). Seismicity in Utah 1850 through June 1965, *Bull. Seismol. Soc. Am.* **57,** no. 4, 689–718.

Crone, A. J., M. N. Machette, M. G. Bonilla, J. J. Lienkaemper, K. L. Pierce, W. E. Scott, and R. C. Bucknam (1987). Surface faulting accompanying the Borah Peak earthquake and segmentation of the lost river fault, central Idaho, *Bull. Seismol. Soc. Am.* **77,** no. 3, 739–770.

Davies, J. H. (2013). Global map of solid Earth surface heat flow, *Geochem. Geophys. Geosys.* **14,** no. 10, 4608–4622.

Dewey, J. W. (1987). Instrumental seismicity of central Idaho, *Bull. Seismol. Soc. Am.* **77,** no. 3, 819–836.

Doser, D. I. (1989). Extensional tectonics in northern Utah southern Idaho, USA, and the 1934 Hansel Valley sequence, *Phys. Earth Planet. In.* **54,** nos. 1/2, 120–134.

DuRoss, C. B., R. D. Gold, T. E. Dawson, K. M. Scharer, K. J. Kendrick, S. O. Akciz, S. J. Angster, J. Bachhuber, S. Bacon, S. E. K. Bennett, *et al.* (2020). Surface displacement distributions for the July 2019 Ridgecrest, California, earthquake ruptures, *Bull. Seismol. Soc. Am.* **110,** no. 4, 1400–1418.

DuRoss, C. B., S. F. Personius, A. J. Crone, S. S. Olig, M. D. Hylland, W. R. Lund, and D. P. Schwartz (2016). Fault segmentation: New concepts from the Wasatch Fault Zone, Utah, USA, *J. Geophys. Res.* **121,** no. 2, 1131–1157.

Evans, J. P., D. C. Martindale, and R. D. Kendrick (2003). Geologic setting of the 1884 Bear Lake, Idaho, earthquake: Rupture in the hanging wall of a basin and range normal fault revealed by historical and geological analyses, *Bull. Seismol. Soc. Am.* **93,** no. 4, 1621–1632.

Farrell, J., R. B. Smith, T. Taira, W. L. Chang, and C. M. Puskas (2010). Dynamics and rapid migration of the energetic 2008-2009 Yellowstone Lake earthquake swarm, *Geophys. Res. Lett.* **37,** 5.

Faulds, J. E., C. D. Henry, and N. H. Hinz (2005). Kinematics of the northern Walker Lane: An incipient transform fault along the Pacific-North American plate boundary, *Geology* **33,** no. 6, 505–508.

Gilbert, H. (2012). Crustal structure and signatures of recent tectonism as influenced by ancient terranes in the western United States, *Geosphere* **8,** no. 1, 141–157.

Haller, K. M., and R. L. Wheeler (2020). Fault number 601c, Lost River fault, Thousand Springs section, Quaternary fault and fold database of the United States, U.S. Geological Survey, available at https://earthquakes.usgs.gov/hazards/qfaults (last accessed March 2020).

Hamilton, W., and W. B. Meyers (1966). Cenozoic tectonics of the western United States, *Rev. Geophys.* **4,** no. 4, 509–549.

Hanks, T. C., and D. P. Schwartz (1987). Morphological dating of the pre-1983 fault scarp on the Lost River fault at Doublespring Pass road, Custer County, Idaho, *Bull. Seismol. Soc. Am.* **77,** no. 3, 837–846.

Hauksson, E., L. M. Jones, and K. Hutton (2002). The 1999 Mw 7.1 Hector Mine, California, earthquake sequence: Complex conjugate strike-slip faulting, *Bull. Seismol. Soc. Am.* **92,** no. 4, 1154–1170.

Koehler, R. D., S. Dee, A. Elliott, A. Hatem, A. Pickering, I. Pierce, and G. Seitz (2021). Field response and surface rupture characteristics of the 2020 M6.5 Monte Cristo Range earthquake, central Walker Lane, Nevada, *Seismol. Res. Lett.* this volume.

Koper, K. D., K. L. Pankow, J. C. Pechmann, J. M. Hale, R. Burlacu, W. L. Yeck, H. M. Benz, R. B. Herrmann, D. T. Trugman, and P. M. Shearer (2018). Afterslip enhanced Aftershock activity during the 2017 earthquake sequence near Sulphur Peak, Idaho, *Geophys. Res. Lett.* **45,** no. 11, 5352–5361.

Kowallis, B. J., J. Ferguson, and G. J. Jorgensen (1990). Uplift along the Salt Lake segment of the Wasatch Fault from apatite and zircon fission-track dating in the Little Cottonwood Stock, *Nucl. Tracks Radiat. Meas.* **17,** no. 3, 325–329.

Kreemer, C., G. Blewitt, and W. C. Hammond (2010). Evidence for an active shear zone in southern Nevada linking the Wasatch fault to the Eastern California shear zone, *Geology* **38,** no. 5, 475–478.

Kuntz, M. A., H. R. Covington, L. J. Schorr, P. K. Link, M. A. Kuntz, and L. B. Piatt (1992). Chapter 12: An overview of basaltic volcanism of the eastern Snake River Plain, Idaho, in *Regional Geology of Eastern Idaho and Western Wyoming*, P.K. Link, M. A. Kuntz, and L. B. Platt (Editors), Geological Society of America, Boulder, Colorado, Vol. 179, 227–267.

Lachenbruch, A. H. (1978). Heat-flow in Basin and Range province and thermal effects of tectonic extension, *Pure Appl. Geophys.* **117,** nos. 1/2, 34–50.

Liberty, L. M., Z. M. Lifton, and T. D. Mikesell (2021). The 32 March 2020 Mw 6.5 Stanley, Idaho earthquake: Seismotectonics and preliminary aftershock analysis, *Seismol. Res. Lett.* this volume, 1–16, doi: 10.1785/0220200319.

Lund, W. R. (2005). Consen\sus preferred recurrence-interval and vertical slip-rate estimates: Review of Utah paleoseismic-trenching data by the Utah Quaternary fault parameters working group, *Utah Geol. Surv. Bull. 134*, 109 pp.

Machette, M. N., S. F. Personius, A. R. Nelson, D. P. Schwartz, and W. R. Lund (1991). The Wasatch fault zone, Utah segmentation and history of Holocene earthquakes, *J. Struct. Geol.* **13,** no. 2, 137–149.

Marone, C., and C. H. Scholz (1988). The depth of seismic faulting and the upper transition from stable to unstable slip regimes, *Geophys. Res. Lett.* **15,** no. 6, 621–624.

Marquardt, D. (1963). An algorithm for least-squares estimation of nonlinear parameters, *SIAM J. Appl. Math.* **11,** 431–441.

McQuarrie, N., and D. W. Rodgers (1998). Subsidence of a volcanic basin by flexure and lower crustal flow: The eastern Snake River Plain, Idaho, *Tectonics* **17,** no. 2, 203–220.

Mohapatra, G. K., and R. A. Johnson (1998). Localization of listric faults at thrust fault ramps beneath the Great Salt Lake Basin, Utah: Evidence from seismic imaging and finite element modeling, *J. Geophys. Res.* **103,** no. B5, 10,047–10,063.

Morgan, W. J. (1972). Plate motions and deep mantle convection, *Geol. Soc. Am. Mem.* Vol. 132, 7–22.

Nevada Seismological Laboratory(NSL) (2020). Mission statement of Nevada seismological laboratory, available at http://www.seismo .unr.edu/About (last accessed July 2020).

Oldow, J. S., J. W. Geissman, and D. F. Stockli (2008). Evolution and strain reorganization within Late Neogene structural stepovers linking the central Walker Lane and northern Eastern California Shear Zone, Western great Basin, *Int. Geol. Rev.* **50,** no. 3, 270–290.

Pang, G. N., K. D. Koper, J. M. Hale, R. Burlacu, J. Farrell, and R. B. Smith (2019). The 2017-2018 Maple Creek earthquake sequence in Yellowstone National Park, USA, *Geophys. Res. Lett.* **46,** no. 9, 4653–4663.

Pang, G. N., K. D. Koper, M. Mesimeri, K. L. Pankow, B. Ben, J. Farrell, J. Holt, J. M. Hale, P. Roberson, R. Burlacu, *et al.* (2020). Seismic analysis of the 2020 Magna, Utah, Earthquake sequence: Evidence for a Listric Wasatch fault, *Geophys. Res. Lett.* **47,** no. 18, 10.

Pang, G. N., K. D. Koper, M. C. Stickney, J. C. Pechmann, R. Burlacu, K. L. Pankow, S. Payne, and H. M. Benz (2018). Seismicity in the Challis, Idaho, Region, January 2014-May 2017: Late Aftershocks of the 1983 Ms 7.3 Borah Peak earthquake, *Seismol. Res. Lett.* **89,** no. 4, 1366–1378.

Pankow, K. L., M. Stickney, J. Y. Ben-Horin, M. Litherland, S. Payne, K. D. Koper, S. L. Bilek, and K. Bogolub (2020). Regional seismic network monitoring in the Eastern Intermountain West, *Seismol. Res. Lett.* **91,** no. 2, 631–646.

Payne, S., A. A. Holland, J. M. Hodges, and R. G. Berg (2005). *INL Seismic Monitoring Annual Report: January 1, 2004 - December 31, 2004*, Idaho National Laboratory, Idaho Falls, Idaho.

Payne, S. J., R. McCaffrey, and S. A. Kattenhorn (2013). Extension-driven right-lateral shear in the Centennial shear zone adjacent to the eastern Snake River Plain, Idaho, *Lithosphere* **5,** no. 4, 407–419.

Petrik, F. E. (2008). Scarp analysis of the Centennial Normal fault, Beaverhead County, Montana and Fremont County, Idaho, *M.S. Thesis*, Montana State University, Bozeman, Montana, 267 pp.

Pierce, K. L., and L. A. Morgan (1992). The track of the Yellowstone hot spot: Volcanism, faulting, and uplift, in *Regional Geology of Eastern Idaho and Western Wyoming*, P.K. Link, M. A. Kuntz, and L. B. Platt (Editors), Geological Society of America Memoir, Boulder, Colorado, Vol. 179, 1–51.

Reynolds, M. W. (1979). Character and extent of Basin-Range faulting, Western Montana and East-Central Idaho, *Rocky Mountain Association of Geologists and Utah Geological Association, 1979 Basin and Range Symposium*, Las Vegas, Nevada, 7–11 October 1979, 185–193.

Richins, W. D., J. C. Pechmann, R. B. Smith, C. J. Langer, S. K. Goter, J. E. Zollweg, and J. J. King (1987). The 1983 Borah Peak, Idaho, earthquake and its aftershocks, *Bull. Seismol. Soc. Am.* **77,** no. 3, 694–723.

Ruhl, C. J., E. A. Morton, M. H.-I. Bormann, G. Ichinose, and K. D. Smith (2021). Complex fault geometry of the 2020 Mw6.5 Monte Cristo Range, Nevada earthquake sequence, *Seismol. Res. Lett.* this volume.

Sbar, M. L., R. B. Smith, C. H. Scholz, M. Barazang, and J. Dorman (1972). Tectonics of Intermountain Seismic Belt, Western United States—Microearthquake seismicity and composite fault plane solutions, *Geol. Soc. Am. Bull.* **83,** no. 1, 13–28.

Scholz, C. H. (1988). The brittle-plastic transition and the depth of seismic faulting, *Geol. Rundsch.* **77,** no. 1, 319–328.

Schwartz, D. P., and K. J. Coppersmith (1984). Fault behavior and characteristic earthquakes—Examples from the Wasatch and San Andreas fault zones, *J. Geophys. Res.* **89,** no. NB7, 5681–5698.

Scott, W. E., K. L. Pierce, and M. H. Hait (1985). Quaternary tectonic setting of the 1983 Borah-Peak earthquake, Central Idaho, *Bull. Seismol. Soc. Am.* **75,** no. 4, 1053–1066.

Shelly, D. R., D. P. Hill, F. Massin, J. Farrell, R. B. Smith, and T. Taira (2013). A fluid-driven earthquake swarm on the margin of the Yellowstone Caldera, *J. Geophys. Res.* **118,** no. 9, 4872–4886.

Shenon, P. J. (1936). The Utah earthquake of March 12, 1934 (extracts from unpublished report), in *United States Earthqakes, 1934*, F. Neuman (Editor), United States Government Printing Office, Washington, D.C., Serial 593, 43–48.

Sibson, R. H. (1982). Fault zone models, heat-flow, and the depth distribution of earthquakes in the continental-crust of the United-States, *Bull. Seismol. Soc. Am.* **72,** no. 1, 151–163.

Smith, R. B., and R. L. Bruhn (1984). Intraplate extensional tectonics of the Eastern Basin-Range—Inferences on structural style from seismic-reflection data, regional tectonics, and thermal-

mechanical models of brittle-ductile deformation, *J. Geophys. Res.* **89,** no. NB7, 5733–5762.

Smith, R. B., and M. L. Sbar (1974). Contemporary tectonics and seismicity of western United States with emphasis on Intermountain Seismic Belt, *Geol. Soc. Am. Bull.* **85,** no. 8, 1205–1218.

Stewart, J. H. (1971). Basin and range structure-System of Horsts and Grabens produced by deep-seated extension, *Geol. Soc. Am. Bull.* **82,** no. 4, 1019–1043.

Stewart, J. H. (1978). Basin and Range structure in western north America: A review, in *Cenozoic Tectonics and Regional Geophysics of the Western Cordillera*, R. B. Smith and G. P. Eaton (Editors), Geological Society of America, Boulder, Colorado, 1–31.

Stickney, M. C., and M. J. Bartholomew (1987). Seismicity and late Quaternary faulting of the Northern basin and range province, Montana and Idaho, *Bull. Seismol. Soc. Am.* **77,** no. 5, 1602–1625.

Thackray, G. D., D. W. Rodgers, and D. Streutker (2013). Holocene scarp on the Sawtooth fault, central Idaho, USA, documented through lidar topographic analysis, *Geology* **41,** no. 6, 639–642.

Thompson, G. A. (1959). Gravity measurements between Hazen and Austin, Nevada: A study of basin-range structure, *J. Geophys. Res.* **64,** no. 2, 217–229.

UNAVCO (2020). Tectonic motions of the Western United States, University NAVSTAR Consortium (UNAVCO) Velocity Map Poster Series, available at https://www.unavco.org/education/outreach/giveaways/velocity-map-posters/velocity-map-posters.html (last accessed July 2020).

U.S. Geological Survey (USGS) (2020a). United States Geological Survey Advanced National Seismic System (ANSS) Comprehensive Earthquake Catalog Event and Products (ComCat), available at https://earthquake.usgs.gov/data/comcat/ (last accessed July 2020).

USGS (2020b). United States Geological Survey Quaternary fault and fold database, available at https://earthquakes.usgs.gov/hazards/qfaults (last accessed July 2020).

Utsu, T. (1961). A statistical study of the occurrence of aftershocks, *Geophys. Mag.* **30,** 521–605.

Utsu, T., Y. Ogata, and R. S. Matsuura (1995). The centenary of the Omori formula for a decay law of aftershock activity, *J. Phys. Earth* **43,** no. 1, 1–33.

Velasco, M. S., R. A. Bennett, R. A. Johnson, and S. Hreinsdottir (2010). Subsurface fault geometries and crustal extension in the eastern Basin and Range Province, western US, *Tectonophysics* **488,** nos. 1/4, 131–142.

Waite, G. P., and R. B. Smith (2002). Seismic evidence for fluid migration accompanying subsidence of the Yellowstone Caldera, *J. Geophys. Res.* **107,** no. B9, 17.

Wells, D. L., and K. J. Coppersmith (1994). New empirical relationships among magnitude, rupture length, rupture width, rupture area, and surface displacement, *Bull. Seismol. Soc. Am.* **84,** no. 4, 974–1002.

Wesnousky, S. G. (2005a). The San Andreas and Walker Lane fault systems, western North America: Transpression, transtension, cumulative slip and the structural evolution of a major transform plate boundary, *J. Struct. Geol.* **27,** no. 8, 1505–1512.

Wesnousky, S. G. (2005b). Active faulting in the Walker Lane, *Tectonics* **24,** no. 3, 35.

Westaway, R., and R. B. Smith (1989). Source parameters of the Cache Valley (Logan), Utah, earthquake of August 30, 1962, *Bull. Seismol. Soc. Am.* **79,** no. 5, 1410–1425.

Witkind, I. J., W. B. Myers, J. B. Hadley, W. Hamilton, and G. D. Fraser (1962). Geologic features of the earthquake at Hebgen Lake, Montana, August 17, 1959, *Bull. Seismol. Soc. Am.* **52,** 163–180.

Working Group on Utah Earthquake Probabilities (WGUEP) (2016). Working group on Utah Earthquake probabilities: Earthquake probabilities for the Wasatch Front region in Utah, Idaho, and Wyoming, *Utah Geol. Surv. Misc. Publ., 16-3,* 164 pp. (165 appendices).

Zeng, Y. H., and Z. K. Shen (2016). A fault-based model for crustal deformation, fault slip rates, and off-fault strain rate in California, *Bull. Seismol. Soc. Am.* **106,** no. 2, 766–784.